Clays and Clay Minerals, Vol. 42, No. 4, 428–436, 1994.

MICROFABRIC OF ALTERED ASH LAYERS, ODP LEG 131, NANKAI TROUGH

JANE S. TRIBBLE[1] AND ROY H. WILKENS[2]

[1] Department of Oceanography, and

[2] Hawaii Institute of Geophysics, School of Ocean and Earth Science and Technology
University of Hawaii, Honolulu, Hawaii 96822

Abstract—Samples of ash layers and associated background sediments from Site 808 of ODP Leg 131 in the Nankai Trough accretionary prism were analyzed for changes in mineralogy, porosity and microfabric associated with alteration of volcanic ash. Ash layers range from incipient stages of alteration and dissolution to complete alteration to clay minerals and clinoptilolite. Ash layers contain greater abundances of total clay minerals and lower percentages of quartz than do surrounding background hemipelagic sediments. The clay-sized fraction of ash layers is dominated by pure dioctahedral smectite, whereas the background sediments contain primarily illite and chlorite with minor amounts of smectite. Analysis of microfabric revealed dramatic changes in the distributions and abundances of grains and pores during ash alteration. The relative abundances of large pores, grains, and matrix material were quantified on digital back-scattered electron images (BSEI) of ash layer and background sediment samples. During burial, the abundant glass shards of shallow ash layers are initially altered, presumably to smectite. Subsequent dissolution of the glass leaves open, shard-shaped pores, resulting in increased porosities. With greater burial, these pores are filled with clinoptilolite. Although the presence of ash and its alteration products clearly influences sediment physical properties, there is no apparent correlation of the abundance of ash or its alteration products with the formation of thrust faults or other structures within the Nankai Trough accretionary prism.

Key Words—Accretionary prism, Alteration, Ash, Microfabric, Nankai Trough, Physical properties, Porosity.

INTRODUCTION

Volcanism associated with subduction contributes a large amount of volcanic ash to forearc regions. Alteration of this ash is a primary source of smectite in accretionary prism sediments (Tribble, 1990). Because of its hydrous nature, smectite can have a large impact on sediment physical properties and mechanical behavior. The high water content of smectite results in a low grain density and low coefficient of friction (Bird, 1984). In the Barbados accretionary prism, the strength contrast between smectite-rich and adjacent smectite-poor units is a major control on location of thrust faults and may influence the location of the basal decollement—the boundary between subducted and accreted sediments (Tribble, 1990; Wilkens *et al.*, 1990).

Loss of smectite interlayer water occurs as a result of both dehydration owing to increased temperature during burial and diagenetic alteration of smectite to illite. Release of water from smectite results in an increase in smectite grain density, an increase in cohesive strength, and dilution of pore waters. Depending on pressure conditions and the relative densities of interlayer vs pore water, transfer of water from interlayer positions to pore spaces may contribute to development of overpressured sediment (Hanshaw and Bredehoeft, 1968; Burst, 1969; Magara, 1975; Bruce, 1984). The presence of smectite, therefore, may determine the timing and extent of dewatering events and the development of structures during accretionary prism evolution.

Because of the important role smectite can play in subduction dynamics, we have investigated the initial formation of smectite via ash alteration and its subsequent diagenesis in accretionary complex sediments. We report here preliminary results of studies of microfabrics associated with volcanic ash alteration and the differences in microfabric between ash-rich and non-ash sediments in samples from the Nankai Trough.

Ocean Drilling Program (ODP) Leg 131, Site 808 is located in the Nankai Trough accretionary complex, at the subduction boundary between the Shikoku Basin and the Southwest Japan Arc (Figure 1). Details of stratigraphy and sediment properties are given in Taira *et al.* (1991). In summary, drilling at Site 808 penetrated a thick section of slope apron sediments that overlies a thicker (>500 m) section of trench wedge turbidites and hemipelagic sediments. A transitional section separates the trench wedge sediments from underlying hemipelagic Shikoku Basin sediments. Ash and tuff layers are common in the transitional section and in the upper 105 m of hemipelagic sediments. A unit of acidic volcaniclastics overlies basaltic basement, encountered at a depth of 1290 mbsf.

In this study mineralogical analyses are reported for 14 background sediments and 11 ash layers from Site 808. The microfabrics of three background sediments

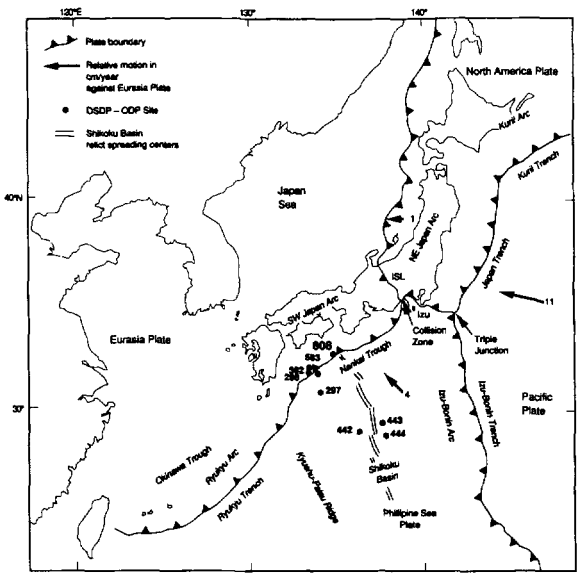

Figure 1. Location of ODP Site 808 in the Nankai Trough where the Philippine Sea Plate is subducted beneath the SW Japan Arc. From Taira *et al.*, 1991.

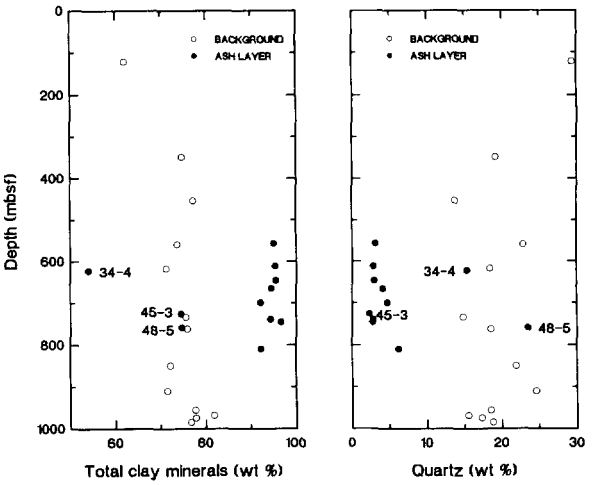

Figure 2. Percentages of total clay minerals and quartz in the bulk sediments from Site 808. In general, ash layers have distinctly higher clay mineral contents and lower quartz concentrations than background sediments. Several exceptions are labeled. Sample 808C-45-3 (725 mbsf) has an unusually high concentration of plagioclase (23%), resulting in a relatively lower clay mineral content (75%). The low concentration of clay minerals in sample 808C-48-5 (75% clay minerals; 759 mbsf) reflects its high quartz content (24%), perhaps as a result of mixing with surrounding background sediment via bioturbation. Sample 808C-34-4 (622 mbsf; 54% total clay minerals; 15% quartz) contains 29% calcite, present primarily as nannofossils, a much higher value than the average calcite content of 3%. On a calcite-free basis, this sample contains 76% total clay minerals and 22% quartz, values similar to those of sample 808C-48-5.

and six ash layers were examined and quantified. The samples are from burial depths of 121–984 mbsf within the trench wedge and hemipelagic section, the transitional unit, and the Shikoku Basin hemipelagics.

ANALYTICAL METHODS

Mineralogy

Mineralogy was determined by X-ray diffraction (XRD) on a Scintag PAD V powder diffractometer. Bulk powders were continuously scanned from 2°–70°2θ at 1°2θ/min, using a chopper increment of 0.03°. Relative abundances of total clay minerals, quartz, plagioclase, and calcite in bulk samples were determined from peak intensities using a simultaneous linear equation algorithm that accounts for peak overlap (Karlak and Burnett, 1966). The quantification routine was calibrated using nine different mixtures of the four phases prepared by combining commercially available standard minerals.

Oriented mounts of the clay-sized (<2 μm) fraction were saturated with ethylene glycol and scanned from 2°–40°2θ at 1°2θ/min and from 59°–63°2θ at 0.25°2θ/min. Estimates of relative abundances of smectite, illite, and the sum of kaolinite plus chlorite were based on peak areas determined using a Scintag profile-fitting routine. Methodologies and weighting factors (WF = 1 for 17 Å smectite peak; WF = 1.8 for 7 Å chlorite + kaolinite peak; WF = 8 for 10 Å illite peak) of Underwood *et al.* (1993) were used. The extent of mixed-layering in the smectite was estimated using shifts in positions of the (001/002) and (002/003) peaks following Moore and Reynolds (1989). No attempt was made in this study to quantify non-crystalline materials such as volcanic glass and biogenic silica, or accessory components such as zeolites.

Scanning electron microscopy (SEM)

Samples taken from Site 808 immediately after recovery were carefully stored in sealed containers with moist sponges to maintain fluid saturation. Pore fluid in 2–3 mm thick slices of the samples was replaced by Spurr low-viscosity epoxy using a step-wise exchange process. The efficacy of the process was confirmed by visual inspection. When the samples were cut and polished, epoxy filled all pore spaces and there was minimal visual damage to sediment fabric. Sections of impregnated sediment samples were polished with 0.25 μm grit and mounted for study with a back-scattered electron detector in a CAMECA microprobe. Back-scattered electron imaging (BSEI) was chosen because examination of polished cross sections is most suitable for quantification of microfabrics and because the sample preparation process eliminates problems of sample dehydration associated with secondary electron imaging of fractured surfaces.

https://doi.org/10.1346/CCMN.1994.0420408 Published online by Cambridge University Press

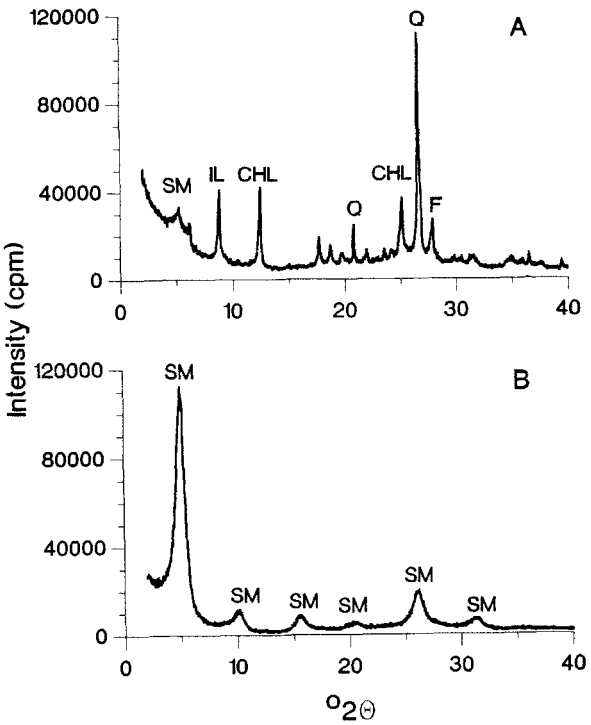

Figure 3. X-ray diffraction patterns of the <2 μm fraction of representative background and ash layer samples. A) Sample 808C-6-2 (349 mbsf) illustrates the mixture of smectite, illite, chlorite, quartz and feldspar typical of background samples. B) The <2 μm fraction of most ash layers is dominated by smectite as illustrated by sample 808C-37-1 (646 mbsf). SM = smectite, IL = illite, CHL = chlorite, Q = quartz, F = feldspar.

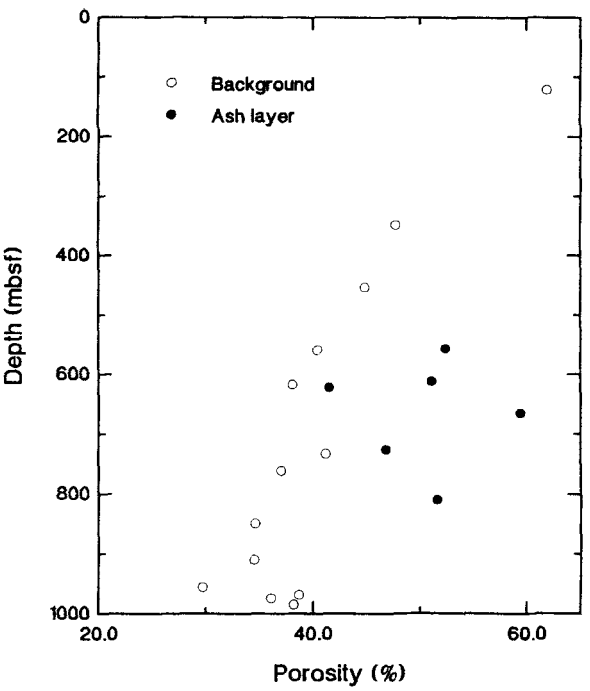

Figure 4. Porosity versus depth for background sediments and ash layers from Site 808. Porosity measurements were made on shipboard on samples from the same core and section and the same lithology as our samples. Measurements from Taira *et al.* (1991).

RESULTS AND DISCUSSION

Mineralogy of background sediments and ash layers

Background sediments from Site 808 are hemipelagic muds and/or turbidites. They contain an average of 75 wt. % total clay minerals, 20 wt. % quartz, 3 wt. % plagioclase, and 3 wt. % calcite. In contrast, ash layers are on average more clay mineral-rich (87 wt. %), and contain less quartz (6 wt. %) (Figure 2). Higher percentages of clay minerals in ash layers reflect both authigenic formation of clay minerals during ash alteration and a lower degree of dilution by terrigenous detritus. Clinoptilolite was also found in all but one sample between 645 and 810 mbsf. Most background samples contain small concentrations of pyroxene, and small quantities of amphibole are present in several background and ash samples at depths less than 740 mbsf.

The mineralogical compositions of the clay-sized fractions of ash layers and background sediments differ significantly (Figure 3). The clay mineralogy of background sediments (Figure 3A) is dominated by illite (an average of 72 wt. %) and chlorite (22 wt. %), with only minor amounts of smectite (6 wt. %). The clay-sized fractions of the ash layers contain an average of 87 wt. % smectite, with minor illite (10 wt. %) and chlorite (3 wt. %), but many are essentially 100 wt. % smectite (Figure 3B). The smectite in the ash layers contains <10% illite interlayers and is dioctahedral. The composition and concentration of smectite in the ash layers are typical of smectite formed authigenically from ash alteration (e.g., Hein and Scholl, 1978). Differences in clay mineralogy between background sediments and ash layers therefore reflect the dominance of a terrigenous source of clay minerals in background sediments vs authigenesis of smectite in ash layers.

The different mineralogical compositions of background sediments and ash layers are reflected in distinctive physical properties. For example, background sediments show a decrease in porosity with depth indicative of "normal" consolidation whereas ash layers maintain high porosities (Figure 4).

Microfabric image processing

SEM observations were made to document contrasts in microfabric between background sediments and ash layers, as well as changes in microfabric associated with alteration of ash components. In addition to qualitative

https://doi.org/10.1346/CCMN.1994.0420408 Published online by Cambridge University Press

observations, digital files of each image were analyzed in a preliminary attempt to quantify our observations. An example of a digital BSEI is shown in Figure 5, a section of sample 808C-27-6. Back-scattered electron intensity is proportional to the bulk density of the area under the electron beam (typically on the order of 1 μm wide). In Figure 5, and in most of the views of the nine samples we examined in detail, there are essentially three elements. Relatively large grains (G) appear uniformly light gray. The grains are surrounded by matrix (M) of a darker hue. The matrix contains much finer grained sediment particles and microporosity. The third element, appearing black in the images, is relatively large pore space (H), now filled with low-density epoxy.

Digital image analysis was used to quantify the volume occupied by the three elements in each image of nine samples from Site 808. Grayscale images were converted to binary (black and white) with thresholds determined interactively by the investigator to identify first only the grains and then only the large pores. The binary images then underwent a "cleaning" process of erosion followed by dilation that removes very small black areas that are not visually identifiable as grains or pores in the raw images (Russ, 1990). Once a cleaned binary image was produced, a simple histogram yielded the percentages of black and white values, and thus a "point-count" of either grains or large pores. Fifty images at two magnifications (200× and 500×) were quantified for the nine samples. Averaged results are listed in Table 1.

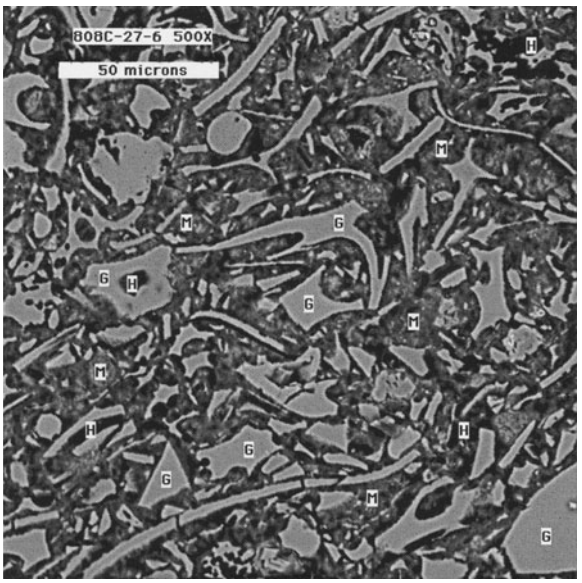

Figure 5. A BSE image of sample 808C-27-6 illustrates the three elements whose abundances were quantified using image analysis techniques. Examples of each element are identified as follows: G = large grains, H = holes (large pore spaces), and M = matrix material.

Microfabric evolution during ash alteration

As expected, one trend observed in the microfabric samples was loss of volcanic glass with depth. Samples 808C-17-1 (453 mbsf) (Figure 6) and 808C-27-6 (557 mbsf) (Figure 5) contain abundant glass shards, al-

Table 1. Quantification of fabric elements, site 808.

Sample, magnification	Description	Depth (msbf)	Total porosity (%)	Grains (%)	Holes (%)	Matrix (%)	Matrix porosity (%)
17-1, 200×	Ash-rich BG	453	44.8	27	3	71	59
17-1, 500×	Ash-rich BG	453	44.8	39	9	53	69
27-6, 200×	Ash	557	52.4	28	3	69	72
27-6, 500×	Ash	557	52.4	35	8	59	76
28-1, 200×	BG	559	40.4	18	4	79	48
28-1, 500×	BG	559	40.4	24	11	66	46
33-4, 200×	Ash	617	51.1	27	4	68	68
33-4, 500×	Ash	617	51.1	31	10	60	70
34-4, 200×	Ash w/ $CaCO_3$	622	41.5	37	3	59	65
34-4, 500×	Ash w/ $CaCO_3$	622	41.5	47	10	44	72
37-1, 200×	Ash	646	NA	9	17	75	NA
37-1, 500×	Ash	646	NA	19	17	65	NA
45-3, 200×	Ash	725	46.8	28	9	63	60
45-3, 500×	Ash	725	46.8	16	13	68	50
49-1, 200×	BG	761	37	25	0	76	49
49-1, 500×	BG	761	37	39	3	59	58
54-1, 200×	Ash	809	51.6	15	1	85	61
54-1, 500×	Ash	809	51.6	19	1	80	63

BG = background.
Total porosity from Taira Hill, Firth *et al.*, 1991.
Matrix = 100% − grains − holes.
Matrix porosity = microporosity within matrix only = (total porosity − holes) × 100/(100 − holes − grains).
NA = not available.

https://doi.org/10.1346/CCMN.1994.0420408 Published online by Cambridge University Press

Figure 6. BSE image of sample 808C-17-1 (453 mbsf) illustrating the abundance of well-preserved glass shards in this ash-rich background sediment.

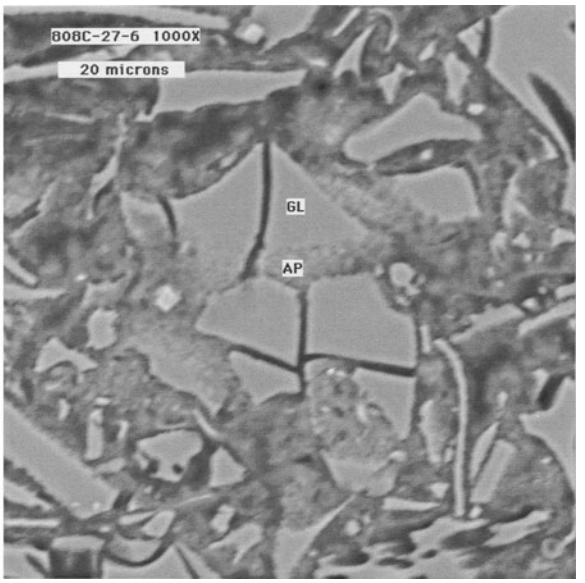

Figure 8. The products of glass alteration (AP), either clay minerals or palagonite, are visible as mottled material associated with the edges of some glass shards (GL) in this BSE image of sample 808C-27-6 (557 mbsf).

though there is evidence for initial alteration of the glass. The edges of typical shards in sample 808C-27-6 are scalloped, indicating dissolution has occurred (Figure 7), and alteration of some shards to clay minerals or palagonite is apparent (Figure 8). The abundance of glass is reflected in relatively high percentages of grains in the 4 shallowest samples (Table 1). In addition to glass, sample 808C-34-4 (622 mbsf) contains abundant nannofossils that contribute to the high percentage of grains (Figure 9; Table 1). In sample 808C-33-4 (617 mbsf), evidence for more progressive dissolution is apparent. Although large glass shards remain, many small shards have been altered or dissolved (Figure 10).

An unusual pattern of porosity, not seen in ash-rich

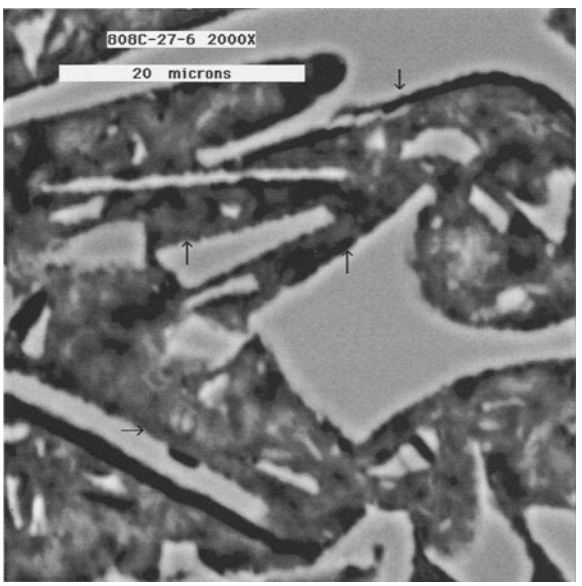

Figure 7. The early stages of volcanic glass alteration are visible in this BSE image of ash layer sample 808C-27-6 (557 mbsf). Edges of glass shards are scalloped (see arrows) indicating an initial stage of glass dissolution. The rims of higher contrast (greater brightness) on all grains are thought to be an artifact resulting from relief created during sample polishing.

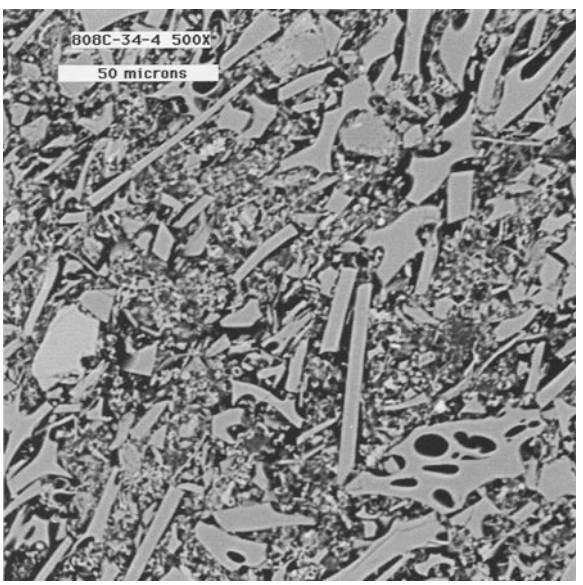

Figure 9. BSE image showing the abundance of nannofossils in sample 808C-34-4 (662 mbsf).

https://doi.org/10.1346/CCMN.1994.0420408 Published online by Cambridge University Press

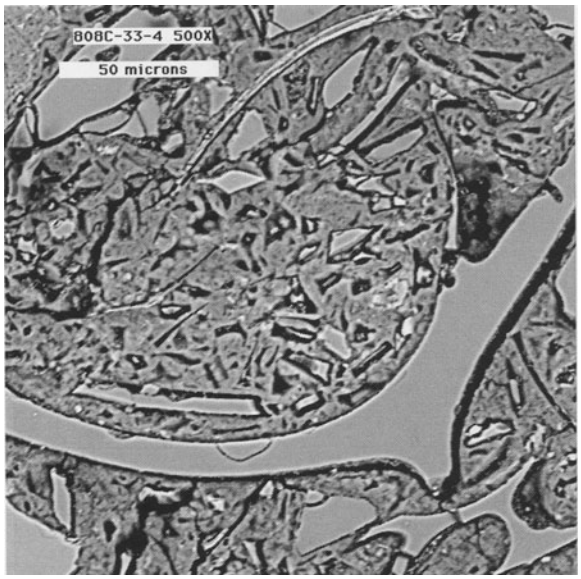

Figure 10. Preferential loss of small glass shards is evident in this BSE image of sample 808C-33-4 (617 mbsf).

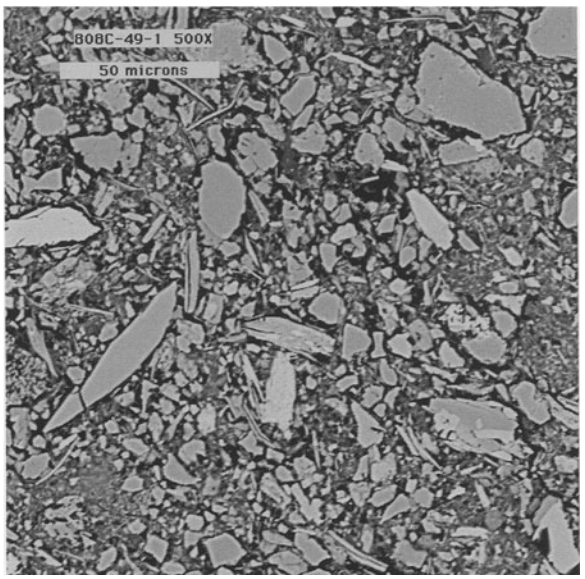

Figure 12. BSE image of background sample 808C-49-1 (761 mbsf). Porosity is lower in background samples than in nearby ash layers and is largely confined to microporosity within the matrix. No large moldic pores similar to those of the ash layers are visible.

or background samples higher in the sediment column, is revealed in sample 808C-37-1 (646 mbsf, Figure 11). Although this sample was identified as being from an ash layer, there is no longer any significant volume of glass grains. Rather, there are pores which maintain shapes very suggestive of glass morphology. These pores, found in several ash samples from below 600 mbsf, constitute 9–17% porosity (Table 1), much greater than in surrounding, normally consolidating background sediment (e.g., sample 808C-49-1, Figure 12). The maintenance of open pores in spite of overburden pressures at burial depths of hundreds of meters suggests

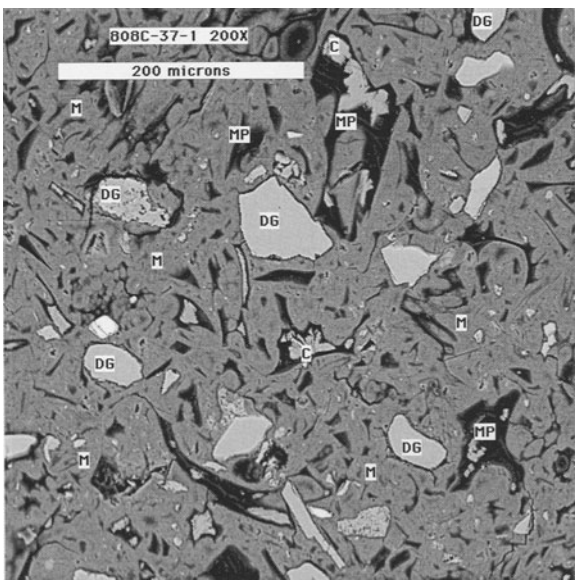

Figure 11. BSE image of ash layer sample 808C-37-1 (646 mbsf) showing the unusual shard-shaped pores created by dissolution of volcanic glass. Some pores have small fragments of glass remaining, and a few are partially filled with clinoptilolite. MP = moldic pores, DG = terrigenous detrital grains, M = matrix, C = clinoptilolite.

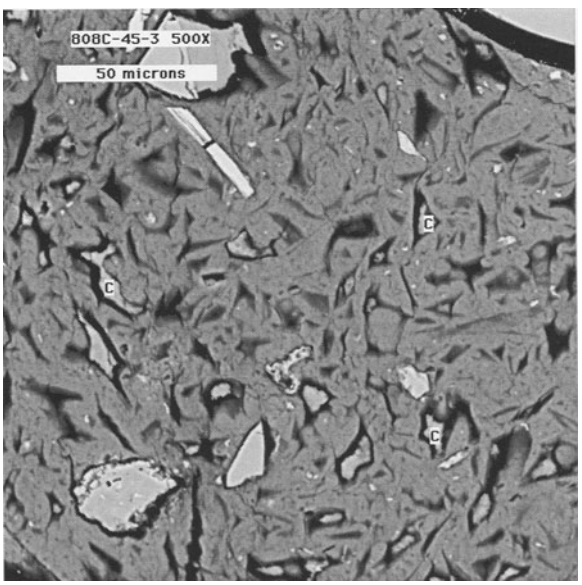

Figure 13. BSE image of ash layer sample 808C-45-3 (725 mbsf) showing abundant moldic pores, some partially filled by clinoptilolite (C).

https://doi.org/10.1346/CCMN.1994.0420408 Published online by Cambridge University Press

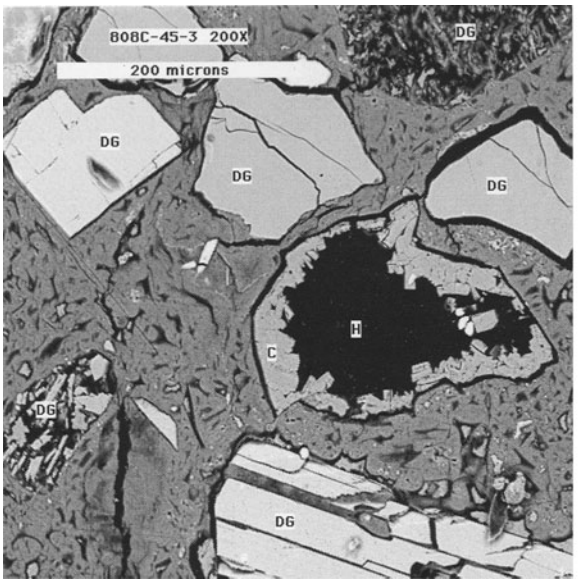

Figure 14. BSE image illustrating precipitation of clinoptilolite (C) in pore space (H) in sample 808C-45-3 (725 mbsf). Clinoptilolite and terrigenous detrital grains (DG) are abundant.

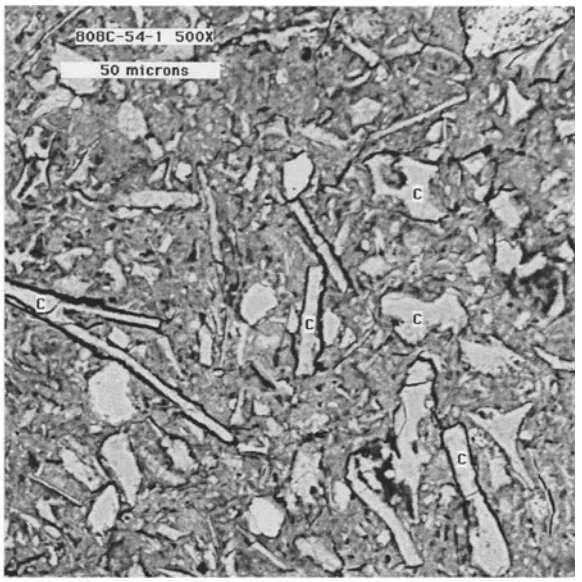

Figure 15. BSE image of ash layer sample 808C-54-1. Large holes are absent and shard-shaped grains are actually filled with clinoptilolite (C).

that dissolution of the glass occurred after the matrix had acquired significant rigidity via compaction and cementation. Sample 808C-45-3 contains similar moldic pores (Figure 13), although numerous pore spaces are infilled by clinoptilolite precipitation (Figure 14). Zeolite and abundant detrital feldspar and lithic fragments account for the anomolously high percentage of grains in this sample (Table 1). Examination of deeper ash layers revealed that zeolite precipitation eventually fills most large pores (Figure 15; sample 808C-54-1).

Contrasts in microfabric and porosity between ash-rich and non-ash sediments

The diagenetic reactions documented above lead to unusual trends in the data of Table 1. During normal consolidation, porosity present both as large holes and as microporosity within the matrix decreases with depth as a result of increased overburden. Also, in the absence of dissolution, the relative percentages of grains and matrix should increase as porosity decreases. Data from Site 808 samples, however, generally do not exhibit the expected trends. Although the measured sample porosity of background sediments decreases with depth, that of the ash layers shows no regular depth trend (Figure 4; Table 1). There is actually a mid-depth maximum in the percentage of holes in the ash layers as a result of dissolution of glass shards and retention of moldic porosity (Table 1). This macroporosity disappears at greater depths as clinoptilolite fills the large pores (sample 808C-54-1, Table 1). Microporosity within the matrix is greater in ash-rich than in background sediments, probably reflecting the higher smectite content of ash layers. The percentage of matrix is similar in all samples.

In addition to differences in abundances of micro- and macroporosity, the shapes and distributions of pores are different in background sediments and ash layers.

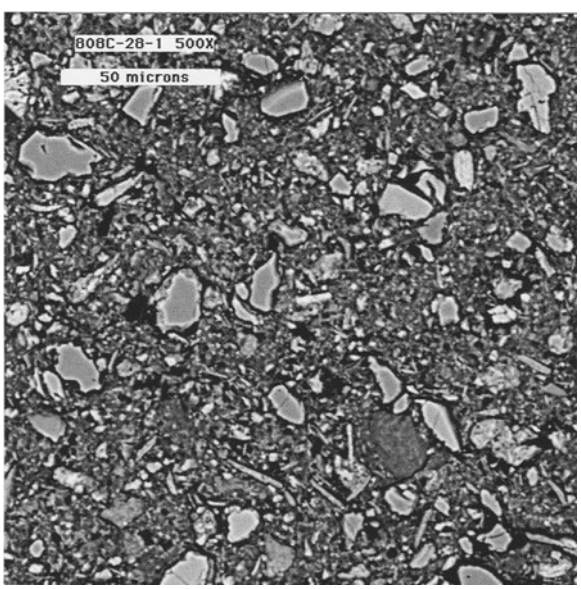

Figure 16. BSE image of background sample 808C-28-1 (559 mbsf) showing the homogeneous distribution of porosity.

https://doi.org/10.1346/CCMN.1994.0420408 Published online by Cambridge University Press

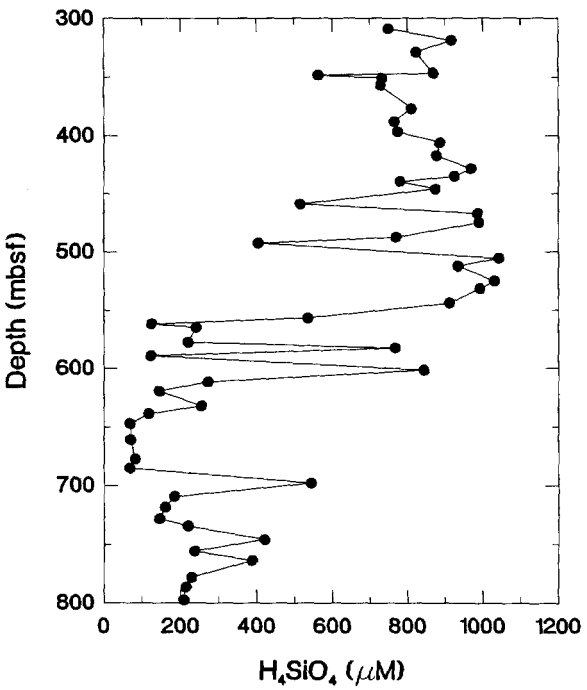

Figure 17. Concentration of silica in pore waters from Site 808 as a function of depth. Data from Taira *et al.*, 1991.

The large pores in unaltered ashes are unevenly distributed and largely associated with vesicles (Figure 5). In contrast, the pores in a nearby background sample (808C-28-1, Figure 16) are more homogeneously distributed. Comparison of a deeper background sample (808C-49-1, Figure 12) and one of the altered ash beds (sample 808C-45-3, Figure 13) illustrates a great contrast in pore shape and size.

CONCLUSIONS

Stages of ash alteration and their effects on porosity, and sediment response to stress

Alteration of volcanic ash in the sediments of the Nankai Trough accretionary prism has resulted in authigenic formation of a smectite-rich matrix and formation of moldic porosity which subsequently is infilled by zeolite precipitation. Diagenesis of the ash appears to proceed in steps. Alteration of glass to smectite occurs early in the process as indicated by the high percentage of smectite in even the most shallowly-buried ash layers. It is likely that precipitation of smectite is fueled by early glass dissolution as evidenced by the scalloped edges of glass shards (Figure 7). Because alteration of volcanic glass to smectite involves net release of dissolved silica to pore waters (Gieskes, 1983), observed high concentrations of dissolved silica at depths less than 560 mbsf probably reflect this early stage of ash alteration (Figure 17, Taira, *et al.*, 1991). These observations are consistent with the two-stage model of diffusion controlled hydration and dissolution of glass followed by first order precipitation of smectite described by Hodder *et al.* (1993).

Wholesale glass dissolution and formation of moldic porosity begin at burial depths greater than 560 mbsf. This depth corresponds to that of the lithologic boundary between trench-fill turbidites and the trench-basin transitional zone. It is also the depth at which the pore water profile of dissolved silica shows a dramatic decrease from values averaging around 900 μM H_4SiO_4 to less than 200 μM H_4SiO_4, although individual ash layers have higher dissolved silica concentrations (Figure 17). This second stage of ash alteration must reflect a new balance between competing reactions involving dissolved silica. Widespread dissolution of glass shards below 560 mbsf should have released high concentrations of silica to solution, even if smectite formation continued. The observed *decrease* of dissolved silica in this section obviously reflects a dominant reaction that acted as a sink for silica. Precipitation of zeolite, the third step in ash alteration, is one possible silica sink. Clinoptilolite was detected by XRD and observed in BSE images at depths as shallow as 646 mbsf. Cementation and/or pore-filling by zeolite or other Si-rich phases may be taking place at shallower depths at a scale too small to be detected by these methods.

The timing of glass dissolution and zeolite precipitation appears to differ from sample to sample. In sample 808C-45-3, clinoptilolite clearly precipitated in previous pore spaces (Figure 14), whereas in sample 808C-54-1, it is possible that some of the zeolite formed by direct replacement of glass without an intervening moldic porosity stage (Figure 15). This direct replacement is suggested by the nearly perfect retention of glass shard morphology. In the moldic pores of shallower samples (e.g., Figures 11 and 13) compaction has tapered the normally blunt terminations of the shard-shaped holes. It is unclear why some glass shards completely dissolved whereas others were replaced. Spatial and/or temporal variations in pore water composition, or differences in glass composition are possible explanations.

The shift from alteration of glass to smectite (stage 1) to widespread dissolution of glass (stage 2) is coincident with the lithologic boundary between trench fill and transitional sediments. The decrease in sedimentation rate associated with this lithologic change (Olafsson, 1993) may be responsible for the change in mode of ash alteration. Dissolution of volcanic ash would proceed more rapidly under the slower depositional rates of the hemipelagic environment where diffusive exchange between pore waters and seawater is more efficient. A similar pattern of glass dissolution leaving shard-shaped pores was observed in pelagic sediments near the Hawaiian Islands (Tribble *et al.*, 1993).

Clinoptilolite precipitation (stage 3) becomes appar-

ent at the boundary between transitional sediments and underlying Shikoku Basin hemipelagics. Limitation of significant clinoptilolite formation to depths greater than 646 mbsf may simply reflect the kinetics of precipitation. Clinoptilolite is not common in young (Pleistocene or Recent), shallowly buried (less than several hundred meters) sediments, especially non-carbonates (Kastner and Stonecipher, 1978). The Nankai Trough section studied here is mostly Pleistocene in age; the Pleistocene-Upper Pliocene boundary is just above 800 mbsf. Rapid sedimentation rates, especially of the overlying trench fill sediments, buried the lowermost Pleistocene and older sediments to the depth range of clinoptilolite formation.

Throughout the different stages of alteration, ash layers maintain physical properties distinctive from those of background sediments. The higher porosities of ash layers are retained (Figure 4), although observations of microfabric document that the nature of porosity changes radically during ash alteration. Although the clay mineral smectite has a high water content and low cohesive strength, the smectite-rich matrix of the ash layers has sufficient strength and rigidity to maintain open pores after glass dissolution at burial depths greater than 560 mbsf.

Alteration of ash may also change the sediment's response to tectonic deformation. Comparison of sediments of the Barbados accretionary complex and the Nankai Trough shows that alteration of volcanic ash is an important source of smectite in sediments of both areas. Volcanic ash and authigenic smectite have a substantial impact on physical properties of sediments from both active margins. Unlike Barbados, however, at Nankai there is no correlation between smectite concentration and location of structures such as thrust faults or the decollement (Taira *et al.*, 1991). Other factors, such as cementation in the sediment matrix and the abundance of sand and silt in the Nankai background sediment, may be playing a more dominant role in determining the sediment's response to tectonic stress.

ACKNOWLEDGMENTS

We thank Michael Underwood and the staff and scientists of ODP Leg 131 for obtaining samples for us. R. Arvidson prepared microfabric samples and assisted in preliminary SEM work. C. Busing assisted in XRD analysis. Reviews by Neal O'Brien and Ray Ferrell, Jr., improved the manuscript. Funding for this work was provided by a JOI/NSF(USSAC) grant and NSF grant OCE-9012145. SOEST Contribution No. 3595.

REFERENCES

Bird, P. (1984) Hydration-phase diagrams and friction of montmorillonite under laboratory and geologic conditions, with implications for shale compaction, slope stability, and strength of fault gauge: *Tectonophys.* **107,** 235–260.

Bruce, C. H. (1984) Smectite dehydration—Its relation to structural development and hydrocarbon accumulation in Northern Gulf of Mexico basin: *Bull. Am. Assoc. Petr. Geol.* **68,** 673–683.

Burst, J. R., Jr. (1969) Diagenesis of Gulf Coast clay sediments and its possible relationships to petroleum migration: *Bull. Am. Assoc. Petr. Geol.* **53,** 73–93.

Gieskes, J. M. (1983) The chemistry of interstitial waters of deep sea sediments: Interpretation of Deep Sea Drilling data: in *Chemical Oceanography 8,* J. P. Riley and R. Chester, eds., Academic Press, New York, 221–269.

Hanshaw, B. B. and Bredehoeft, J. D. (1968) On the maintenance of anomalous fluid pressures II; source layer at depth: *Geol. Soc. Am. Bull.* **79,** 1107–1122.

Hein, J. R., and Scholl, D. W. (1978) Diagenesis and distribution of late Cenozoic volcanic sediment in the southern Bering Sea: *Geol. Soc. Am. Bull.* **89,** 197–210.

Hodder, A. P. W., Naish, T. R., and Nelson, C. S. (1993) A two-stage model for the formation of smectite from detrital volcanic glass under shallow-marine conditions: *Mar. Geol.* **109,** 279–285.

Karlak, R. F. and Burnett, D. S. (1966) Quantitative phase analysis by X-ray diffraction: *Anal. Chem.* **38,** 1741–1745.

Kastner, M. and Stonecipher, S. A. (1978) Zeolites in pelagic sediments of the Atlantic, Pacific, and Indian Oceans: in *Natural Zeolites, Occurrence, Properties, Use,* L. B. Sand and F. A. Mumpton, eds., Pergamon Press, New York, 199–220.

Magara, K. (1975) Reevaluation of montmorillonite dehydration as cause of abnormal pressure and hydrocarbon migration: *Bull. Am. Assoc. Petr. Geol.* **59,** 292–302.

Moore, D. and Reynolds, R. (1989) *X-Ray Diffraction and the Identification and Analysis of Clay Minerals:* Oxford University Press, New York, 332 pp.

Olafsson, G. (1993) Calcareous nannofossil biostratigraphy of the Nankai Trough: in *Proc. ODP, Sci. Results, 131,* I. A. Hill, A. Taira, J. V. Firth *et al.,* eds., Ocean Drilling Program, College Station, Texas, 3–13.

Russ, J. C. (1990) *Computer-Assisted Microscopy:* Plenum Press, New York, 453 pp.

Taira, A., Hill, I., and Firth, J. V. (1991) *Proc. ODP, Init. Repts., 131,* Ocean Drilling Program, College Station, Texas 434 pp.

Tribble, J. S. (1990) Clay diagenesis in the Barbados accretionary complex: Potential impact on hydrology and subduction dynamics: in *Proc. ODP, Sci. Res., 110,* J. C. Moore, A. Mascle *et al.,* eds., Ocean Drilling Program, College Station, Texas, 97–110.

Tribble, J. S., Wilkens, R. H., and Sasaki, S. (1993) Changes in microfabric associated with alteration of volcanic ash: A comparison of the Nankai Trough, Hawaiian Arch, and Barbados accetionary complex: *EOS* **74,** 226.

Underwood, M., Orr, R., Pickering, K., and Taira, A. (1993) Provenance and dispersal patterns for sediments in the turbidite wedge of Nankai Trough: in *Proc. ODP, Sci. Results, 131,* I. A. Hill, A. Taira, J. V. Firth *et al.,* eds., Ocean Drilling Program, College Station, Texas, 15–33.

Wilkens, R. H., McClellan, P., Moran, K., Tribble, J. S., Taylor, E., and Verduzco, E. (1990) Diagenesis and dewatering of clay-rich sediments, Barbados accretionary prism: in *Proc. ODP, Sci. Res., 110,* J. C. Moore, A. Mascle *et al.,* eds., Ocean Drilling Program, College Station, Texas, 309–320.

(Received 29 April 1993; accepted 18 March 1994; Ms. 2373)